Chinese Journal of Chemical Engineering 83 (2025) 137–147

Contents lists available at ScienceDirect

Chinese Journal of Chemical Engineering

journal homepage: www.elsevier.com/locate/CJChE

Full Length Article

Removal of deposited metal particles on a horizontal surface by vertical submerged impinging jets

Han Peng [1], Xinliang Jia [2,3], Xiaofang Guo [2,3], Yubo Jiang [2,3], Zhipeng Li [1,*], Zhengming Gao [1,*], J.J. Derksen [4]

[1] State Key Laboratory of Chemical Resource Engineering, School of Chemical Engineering, Beijing University of Chemical Technology, Beijing 100029, China
[2] China Nuclear Power Engineering Co., Ltd., Beijing 100840, China
[3] Innovation Center for Nuclear Facilities Decommissioning and Radioactive Waste Management Technology, Beijing 100840, China
[4] School of Engineering, University of Aberdeen, Aberdeen AB24 3UE, UK

ARTICLE INFO

Article history:
Received 18 December 2024
Received in revised form
8 February 2025
Accepted 20 February 2025
Available online 22 March 2025

Keywords:
Particle removal
Impinging jet
Shields number
Computational fluid dynamics
Two-phase flow
Transport

ABSTRACT

Jet agitation is known as a maintenance-free stirring technique for nuclear wastewater treatment and demonstrates great potential in transport of radioactive particles. Removal processes of horizontal sediment beds driven by impinging jets were experimentally investigated using image capture and processing technique. The beds were composed of heavy fine particles with particle density ranging from 3700 to 12600 kg·m^{-3} and particle diameter from 5 to 100 μm. The jet Reynolds number varied between 4300 and 9600. The single-phase large eddy simulation method was used for calculating both jet flow characteristics and wall shear stresses. The effects of jet strength, particle density, particle diameter, and bed thickness on bed mobility in terms of the critical Shields numbers were considered. Specifically, the critical Shields number was found to be intricately related to properties of particles, and independent of jet intensity. A new Shields number curve for stainless-steel particles was found, and a model was proposed to predict the transport rate of thin beds, with $R^2 = 0.96$.

1. Introduction

Jet agitators are widely applied for solids suspension processes in large nuclear waste storage tanks [1–3]. Generally, the radioactive particles are too heavy to be uniformly suspended in tanks. The key to design these jet agitators lies in predicting the cleaning efficiency of the jet on the bottom wall. For noncohesive particles, their motion is mainly determined by the competition between the shear stress of liquid flow and the net mass of particles. This competition is reflected in the dimensionless Shields number [4]: $\theta = \tau/[g(\rho_s - \rho)d]$, where τ is the shear stress at the bed surface, g is the gravitational acceleration, ρ_s is the particle density, ρ is the liquid density, and d is the average particle size. Further, the critical Shields number [5] is used to predict the incipient bed motion: $\theta_c \equiv \tau_c/[g(\rho_s - \rho)d]$, where τ_c is the critical shear stress. That is, the critical Shields number reflects the ease with which particle motion is initiated. When the Shields number reaches its critical value, particles begin to exhibit initial motion. This provides a quantitative basis for predicting key phenomena such as particle transport initiation and bed layer changes. Other dimensionless groups also play significant roles in the cleaning process. The jet Reynolds number Re_j quantifies the velocity of jet, and the particle Reynolds number Re_p reflects the ratio of the inertia force to the viscous force acting on particles.

Extensive experimental studies on cleaning efficiency of jets have been reported. Young *et al.* [6] measured the wall shear stress exerted by impinging jets and proposed a correlation between wall shear stress and removal of sparsely distributed particles. Wilson *et al.* [7] got a simple function between the cleaning radius of jets and time. Wall shear stress is an important parameter for calculating the driving force of particles, but experimental measurement of the wall shear stress exerted by impinging jets is challenging. An optical method such as particle image velocimetry (PIV), is incompetent to resolve the near-wall shear flows due to the limits on spatial resolution [8]. Phares *et al.* [9] proposed that the electrochemical method exhibited the highest accuracy among the common indirect methods for measuring the wall shear stress. Electrochemical diffusion techniques have been employed in recent studies exploring the characteristic of impinging jet flow [10–12].

* Corresponding authors.
E-mail addresses: lizp@mail.buct.edu.cn (Z. Li), gaozm@mail.buct.edu.cn (Z. Gao).

https://doi.org/10.1016/j.cjche.2025.02.017
1004-9541/© 2025

Apart from experimental techniques, computational fluid dynamics (CFD) simulations offer an alternative means of obtaining wall shear stresses. Eisner [13] used CFD simulations to calculate the wall shear stresses exerted by impinging jets, and the results of an unpaired, two-tailed t-test (with a significance level of $P < 0.05$) indicated no statistically significant difference between simulated and experimental data.

In this study, an experimental setup for submerged impinging jets was established. The first aim of this study is to validate the CFD simulations for predicting the single-phase impinging jet flow characteristics. It is achieved by comparing the simulated velocities and wall shear stresses with those reported in the literature. The second aim is to identify the key factors influencing the removal process of sediment bed under impinging jets. A series of heavy particles made of metals with densities larger than 8000 kg·m^{-3} were used to form beds, which has not been reported before.

The rest of this study is organized as follows. The parameters of the flow system are detailed in Section 2, including jet flow rates and properties of particles. Then in next section, the CFD methodology is summarized, and the simulations are verified. In the results section (Section 4), we show the effects of jet intensity, particle density, particle diameter and bed thickness on the removal processes. Along with a corrected coefficient, the model proposed in this study is valid for the prediction of transport rates of thin beds. The last section summarizes the key findings of this study and discusses the direction of future research.

2. Experimental

2.1. Flow system

The jet flow configuration is sketched in Fig. 1. A square glass tank is used with a side length L of 0.22 m and a liquid height H of 0.23 m. The jets are from a smooth glass circular tube with an inner diameter D of 0.005 m, an outer diameter D_o of 0.008 m, and a length of 0.3 m. The distance from tube outlet to bottom wall is constant and equal to 0.05 m. Deionized water fills the tank. Its temperature is maintained at 20 °C ± 1 °C, with an estimated density ρ of 1000 kg·m^{-3} and a dynamic viscosity μ of 0.001 kg·m^{-1}·s^{-1}.

The characteristics of jets are determined by their jet Reynolds numbers $Re_j = \rho u_0 D/\mu$, where u_0 is the mean flow velocity within the tube. The Reynolds numbers Re_j varies between 4260, 6530, and 9570, corresponding to flow rates of 60, 92.6, and 135 L·h^{-1}, respectively. The flow rates were measured by weighing the mass of outlet liquid per unit time, with error within ±1%.

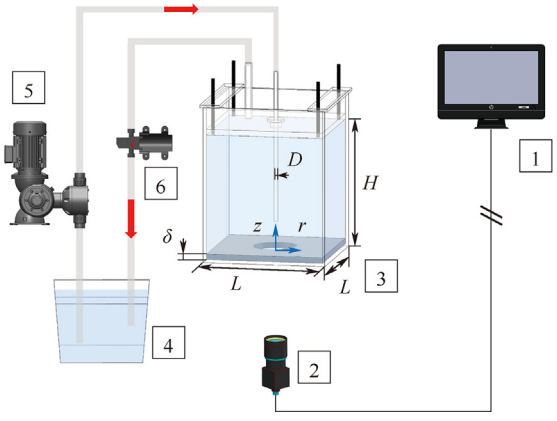

Fig. 1. Experimental setup: 1— computer, 2— camera, 3— jet system, 4— water storage tank, 5— metering pump, 6— circulating pump.

A LCA1-M910S metering pump (LEWA, Germany) provided stable jet flows, with flow fluctuations less than ±3%. The circulating pump 6 in Fig. 1 kept the constant liquid height. To record the temporal evolutions of the cleaned areas, a GO-5000M-USB camera (JAI, Denmark), of 2592 pixels × 1944 pixels resolution with pixel size of 66 × 66 μm^2, was placed below the glass tank, as shown in Fig. 1. Considering lens distortion, the error in size measurement was kept within ±0.5%.

Before each experiment, a particle bed with an initial thickness δ ranging from 0.0003 to 0.007 m was uniformly spread on the bottom wall by using a special scraper. The metering pump 5 and circulating pump 6 were started sequentially, as shown in Fig. 1. Under the action of jet, a cleaned area appeared, and the evolution of its radius over time was recorded by camera [2].

2.2. Particle properties

The six kinds of particles used to form the beds in the experiments are listed in Table 1. The particle density ρ_s ranges from 3700 to 12600 kg·m^{-3}, and the particle diameter d ranges from 5 to 100 μm. The particle densities were measured by hydrostatic weighing method, with error within ±1%. Among the particles, those with a diameter of 5 μm exhibit irregular shapes due to manufacture limitations, while the other particles are approximately spherical, with some of them shown in Fig. 2. The dimensionless submerged specific weight of sediment s is defined as $\rho_s/\rho - 1$.

3. Numerical Methods and Validation

In this section, we show the large eddy simulation (LES) method for predicting the single-phase jet flow first, and then we validate the simulations by using the experimental data on velocities and wall shear strain rates from the Ref. [12].

3.1. Large eddy simulation

The fundamental equations guiding LES for incompressible fluids are the Navier–Stokes equations and continuity equations, both of which have undergone filtering.

$$\frac{\partial \overline{u}_i}{\partial t} + \frac{\partial \overline{u}_i \overline{u}_j}{\partial x_j} = -\frac{1}{\rho}\frac{\partial \overline{p}}{\partial x_i} + \nu \frac{\partial^2 \overline{u}_i}{\partial x_j \partial x_j} - \frac{\partial \sigma_{ij}}{\partial x_j} \tag{1}$$

$$\frac{\partial \overline{u}_i}{\partial x_i} = 0 \tag{2}$$

where u is the velocity component, i and j are the coordinate directions, t is the time, p is the pressure, ν is the kinematic viscosity, σ is the sub-grid scale stress tensor, and the overbars denote the filtered variable on resolved scales.

Table 1
Properties of particles used in the experiments.

Material	Diameter/μm	s	Shape
Aluminum oxide	100 ± 5	2.70	Spherical
Stainless steel	5 (average)	7.04	Irregular
Stainless steel	20 ± 5	7.04	Spherical
Stainless steel	50 ± 5	7.04	Spherical
Stainless steel	100 ± 5	7.04	Spherical
Tungsten carbide	100 ± 5	11.6	Spherical

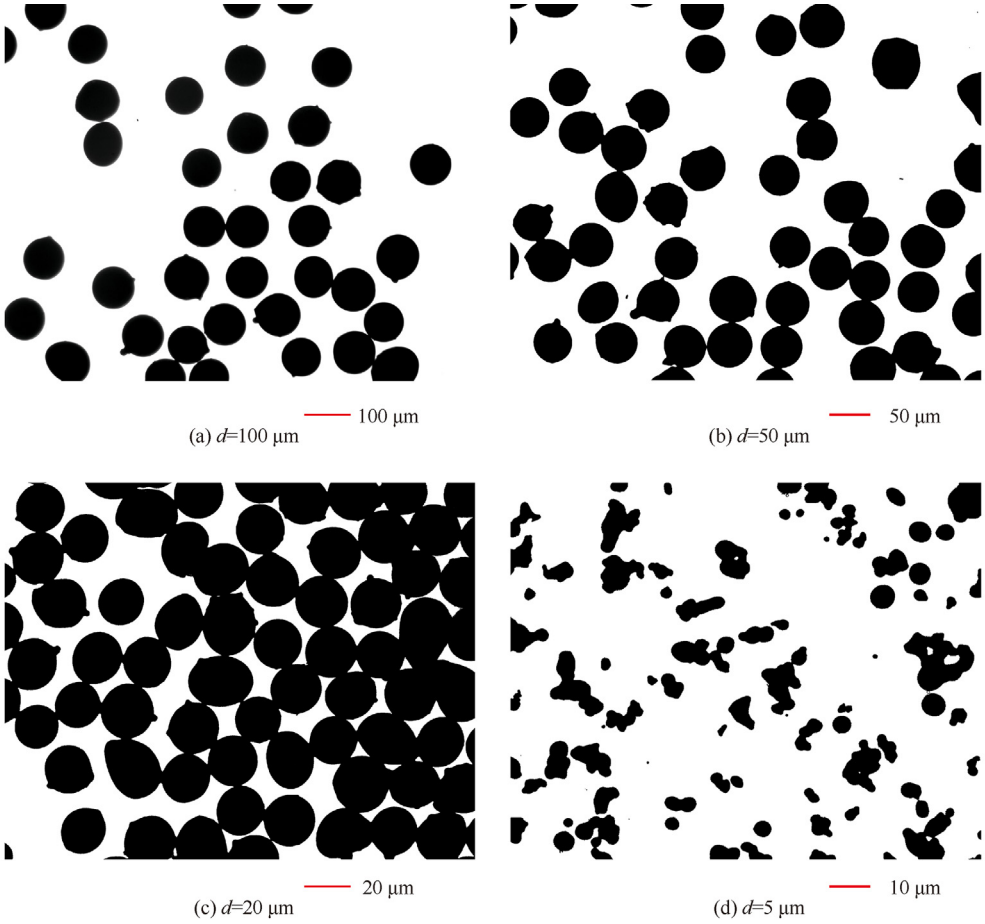

Fig. 2. Morphology of stainless-steel particles with average diameter of (a) 100 μm; (b) 50 μm; (c) 20 μm; (d) 5 μm, as captured by a MIT1818072 metallographic microscope (CNOPTEC, China).

After filtering by the resolved scale grid, the effect of filtering is represented by the sub-grid scale stress tensor

$$\sigma_{ij} = \overline{u_i u_j} - \overline{u}_i \overline{u}_j \tag{3}$$

Based on the eddy-viscosity assumption in most sub-grid scale models, the sub-grid scale stress tensor is modeled as

$$\sigma_{ij} - \frac{1}{3}\delta_{ij}\sigma_{kk} = -2\nu_t \overline{S}_{ij} \tag{4}$$

where δ_{ij} is the Kronecker delta, ν_t is the eddy viscosity, and the deformation tensor of the resolved field is

$$\overline{S}_{ij} = \frac{1}{2}\left(\frac{\partial \overline{u}_i}{\partial x_j} + \frac{\partial \overline{u}_j}{\partial x_i}\right) \tag{5}$$

The wall-adapting local eddy-viscosity (WALE) model [14] is designed to predict near-wall flow characteristics and correctly handle the laminar-to-turbulent transition processes. The model produces zero eddy viscosity in the vicinity of a wall so that no damping function is needed to compute wall bounded flows. Moreover, the high-resolution requirements for wall boundary layers result in the WALE model being recommended only when near-wall flows are important [15]. The eddy viscosity is modeled by

$$\nu_t = (\min(\kappa y, C_w \Delta))^2 \frac{\left(S_{ij}^d S_{ij}^d\right)^{3/2}}{\left(\overline{S}_{ij}\overline{S}_{ij}\right)^{5/2} + \left(S_{ij}^d S_{ij}^d\right)^{5/4}} \tag{6}$$

$$S_{ij}^d = \frac{1}{2}\left(\overline{g}_{ij}^2 + \overline{g}_{ji}^2\right) - \frac{1}{3}\delta_{ij}\overline{g}_{kk}^2, \quad \overline{g}_{ij} = \frac{\partial \overline{u}_i}{\partial x_j} \tag{7}$$

where $\kappa = 0.41$ is the von Karman constant, y is the distance to the closest wall, $C_w = 0.325$ is a coefficient, $\Delta = V^{1/3}$ is the filter width, V is the cell volume, and S_{ij}^d is the traceless symmetric part of the square of the velocity gradient tensor.

All parameters and operating conditions in the simulations are set as they are in the experiments. A uniform velocity inlet is located at the top of the tube, and a uniform pressure outlet is situated on the top surface of the tank. The wall boundary condition is set as no-slip.

Structured, nonuniformly distributed hexahedral grids are used. Although the WALE model is a yplus-insensitive wall treatment model [14], we set up the boundary layer grids on both tube inner wall and tank bottom wall. The dimensionless wall distance $y^+ = \rho y U_f/\mu$ remains around 1 for the cell closest to the wall, $U_f = \sqrt{\tau/\rho}$ is the friction velocity, and τ is the wall shear stress. In fact, we cannot know the value of y^+ except from the simulation results. If y^+ is greater than expected, a new and finer boundary layer grid is required.

The Courant–Friedrichs–Lewy (CFL) number serves as a criterion for assessing the stability of simulations, and is defined as $u\Delta t/\Delta x$, where the Δt is time step of the simulation, Δx is the grid spacing. With maximum grid spacing $\Delta x_{max} \leq 0.0004$ m and CFL $\leq$ 2.0, the simulated results in Section 4 are grid independent, see Fig. S1 in the Supplementary Material. These criteria are used for all the simulations. Data sampling begins when the average pressure on the sidewall of the tank is stable. The total sampling time for each simulation is 5 s, during which time the jet traverses the study area ($r/D \leq 15$) at least 20 times.

The ANSYS Fluent 2022R1 software [15] is used to simulate the jet flow. The coupling between pressure and velocity is accomplished by the semi-implicit method for pressure linked equations. For the spatial discretization of the momentum equations, the central differencing scheme is employed, while the second-order implicit scheme is utilized for the transient formulation.

3.2. Simulation validation

To support the validity of simulations in this study, we cited extensive data from the literature [12] on velocities and wall shear strain rates of jets from three round orifice nozzles. The impinging jet and the measurement plane are schematically shown in Fig. 3(a). The velocity profiles at $z/D = 0.3$ and wall shear strain rate profiles at $z/D = 0$ were measured by using PIV and electrochemical diffusion technique, respectively.

Fig. 3(b) displays a schematic diagram of three nozzles used. The numerical model and details are the same as those in Section 3.1. Three dimensional geometric parameters and operation conditions in the simulations are set as they are in the Ref. [12], with a jet Reynolds number Re_j of 5620. We started the simulations from stationary status and began to collect time-averaged velocity field when the jet stabilized.

The profiles of simulated and experimental streamwise velocity u_z are given in Fig. 4(a), and they all exhibit M shapes. Sodjavi *et al.* [12] attributed this flow deceleration in the core region to the high static pressure at the impact point ($x/D = 0$, $z/D = 0$) [12]. Simulations yield results close to experimental values when predicting transverse velocity u_x, as shown in Fig. 4(b). Given that the maximum deviation at the core of jets is less than 8% in both figures, the simulated results match well with the experimental data.

Besides the velocity, the profiles of wall shear strain rate $\gamma = \tau/\mu$ are given in Fig. 4(c), which are obtained by using three nozzles. Along the direction away from the impact point, the shear strain rates decrease after reaching the peak values. The simulated wall shear strain rates are within ±9% of the ones measured. The accuracy of WALE LES model in calculating impinging jet flow field has been confirmed. Compared with the WALE LES model, three Reynolds averaged Navier–Stokes (RANS) turbulence models all overestimate the wall shear strain rates when $r/D > 1.5$, as shown in Fig. 4(d).

4. Results and Discussion

4.1. Interaction process between jets and particles

Based on our visual observations, the impinging jet swept particles from the center into the surrounding region. The photographs of the particle bed, captured by the camera below the bottom wall at the time points when the jet lasted for 10 s, 20 s, and 30 s, are presented in Fig. 5. By image processing using the circle Hough transform [16] method, we recognize and record the cleaned areas as dashed lines shown in Fig. 5. There is no particle inside the red circles, and the radii of circles are called the removal radii.

Fig. 5(d) shows a steady bed, with its radius considered as the critical removal radius. To ensure that the beds reach a stable

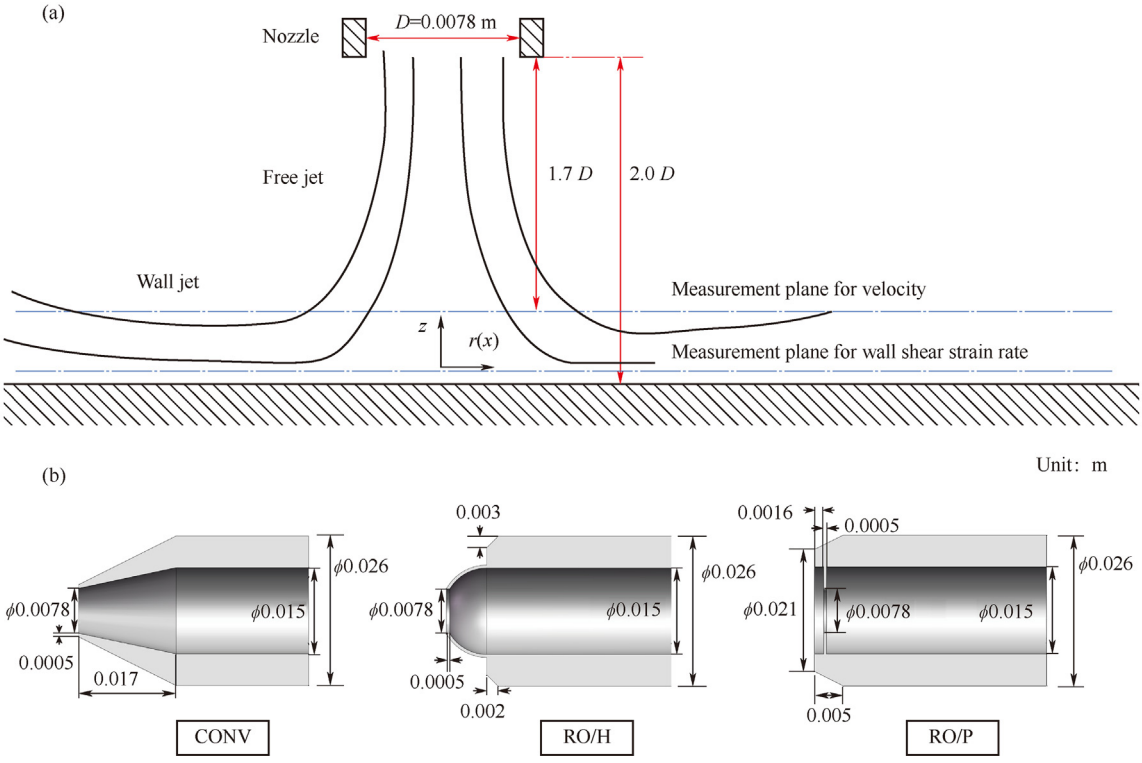

Fig. 3. Schematic description of (a) impinging jet and (b) three nozzles: convergent nozzle (CONV), round orifice on hemisphere (RO/H), and round orifice on plate (RO/P) [12].

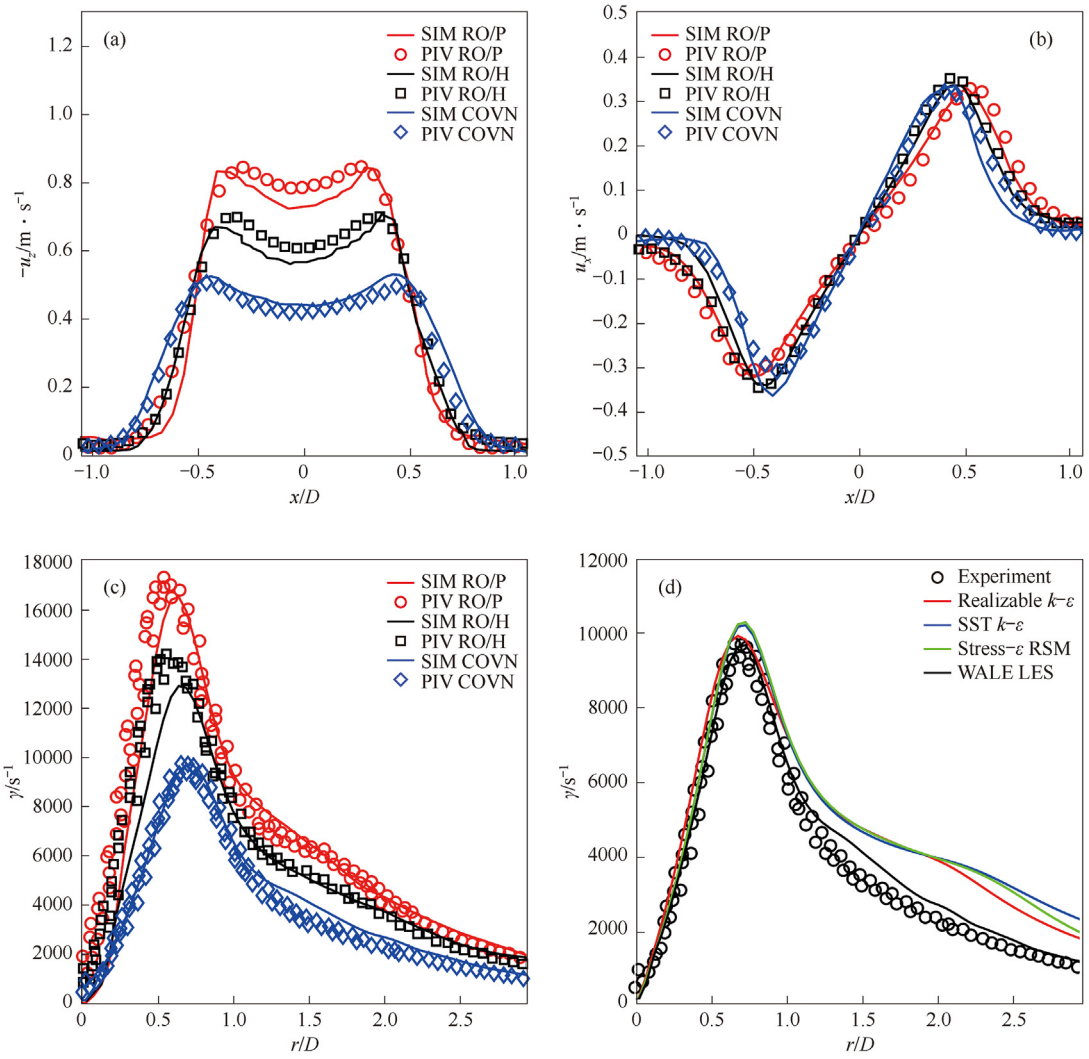

Fig. 4. Velocity profiles ($z/D = 0.3$) obtained by LES and PIV along the (a) streamwise direction, and (b) transverse direction. Wall shear strain rate profiles ($z/D = 0$) obtained by LES and electrochemical diffusion technique (c) by using the three nozzles as shown in Fig. 3(b), and (d) by simulations with four models for the COVN nozzle.

state, the duration of the jets must be sufficiently long. We selected a working time of 5000 s, balancing the accuracy against the time cost of experiments, given that the differences between radii at 4000 s and 5000 s were less than 3% for all beds considered.

4.2. Effect of jet intensity

In this section, we will discuss the effect of jet intensity on the critical Shields numbers of particles, starting with a description of the jet flow field.

With the diameter of the tube outlet as the characteristic size, the Rej were set to 4260, 6530, and 9570. The profiles of dimensionless velocity u_z/u_0 at distance from the wall $z/D = 0.25$ and $z/D = 9.75$ are shown in Fig. 6(a). The profiles are nearly identical beyond the core region ($r/D < 0.5$) at different Rej, which reveals the similarity in flow characteristics.

Shear stress is a significant driving force for the motion of non-cohesive particles in the shear flow [17]. Given that there were no particles in the cleaned area and only a few at the removal radius (see the base of dune in Fig. 5(d)), the wall shear stress from single-phase LES simulation is a good estimate of the shear stress on particles at the removal radius. The profiles of wall shear strain rates obtained by using the LES method are shown in Fig. 6(b), and some bumps are noticed around $r/D = 2$. Meslem *et al.* [18] reviewed relevant studies and found that the curves of wall shear strain rates were smooth when $Re_j < 2000$. Tummers *et al.* [19] attributed these bumps to flow reversal. We plot the flow field near the wall at the position of the green dashed line when $Re_j = 4260$, and confirm the existence of flow reversal.

The temporal evolutions of bed removal radii r in experiments are given in Fig. 6(c). Beds moved fast near the impact point and then gradually stabilized. The critical removal radii of beds are recorded at $t = 5000$ s, and are positively correlated with the Rej.

Fig. 6(d) is a partial enlargement of Fig. 6(b). Taking the three r/D positions of critical removal radii in Fig. 6(c) as horizontal coordinates, we mark the three critical shear strain rates corresponding to three Rej with green dashed lines, and find that they are each approximately 350 s. The critical Shields number can be calculated using the equation $\theta_c = \tau_c/[g(\rho_s - \rho)d] = \mu\gamma_c/[g(\rho_s - \rho)d] \approx 0.0509$, which is in agreement with the critical Shields number of 0.05 for sand on a horizontal bed estimated by Fredsøe *et al.* [20]. It means that the jet intensity has very little effect on the critical Shields number.

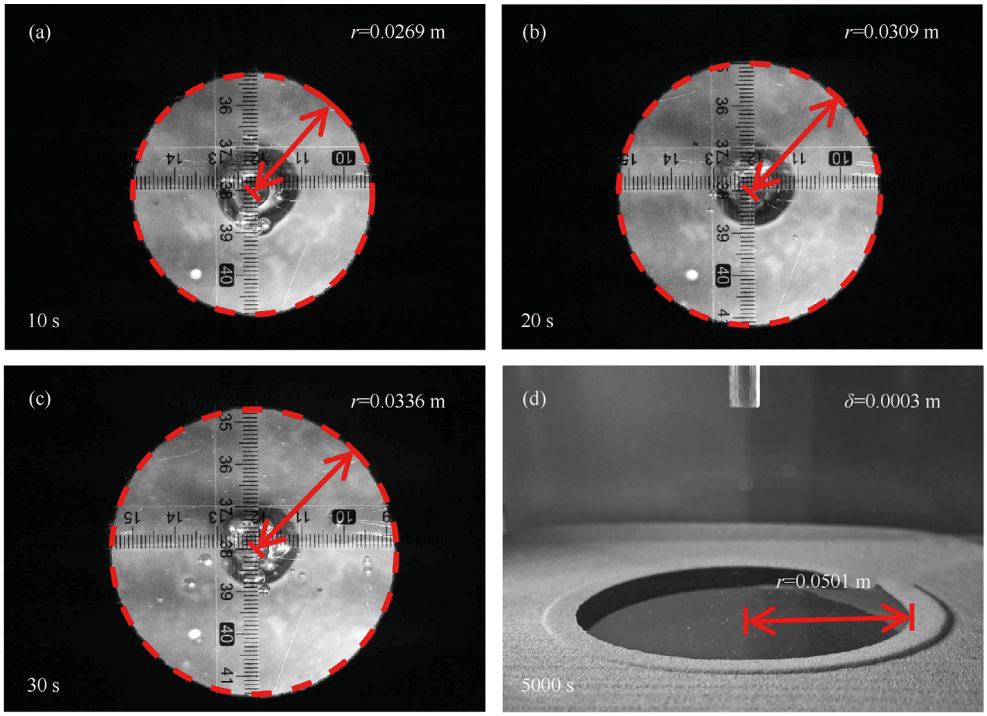

Fig. 5. Photographs of beds from the bottom view at (a) 10 s; (b) 20 s; (c) 30 s. (d) Photograph of steady bed from the side view at 5000 s (Re_j = 6530, s = 7.04, d = 100 μm, δ = 0.0003 m).

4.3. Effect of particle property

Three materials were selected for the particles, namely alumina (s = 2.70), stainless steel (s = 7.04), and tungsten carbide (s = 11.6). With a Rej of 6530, an average particle diameter of 100 μm, and an initial bed thickness of 0.0003 m, the temporal evolutions of bed removal radii in the experiments are presented in Fig. 7(a). As the particle densities increase, the critical removal radii of beds decrease.

The particle diameter is another variable when calculating the Shields number. Four kinds of stainless-steel particles were selected as the research objects, and their average diameters were 5, 20, 50, and 100 μm, respectively. With an initial bed thickness of 0.0003 m and a Rej of 6530, the experimental results are shown in Fig. 7(b). In comparison with particle density, the diameter of particle has less effect on the critical removal radius.

It is interesting to note that smaller density and smaller diameter shorten the time the beds take to reach stability in Fig. 7. This might be that their smaller inertia enables the particles to respond more rapidly to shear stresses, especially those stresses slightly above the critical shear stresses.

To model the relation between particle properties and critical Shields numbers, Cao *et al.* [21] defined the particle Reynolds number $Re_p = d\sqrt{sgd}/\nu$ and reported that the critical Shields number θ_c was negatively correlated with the particle Reynolds number when $Re_p < 65$, based on the research results of Yalin *et al.* [22].

According to our experimental results in Fig. 7, the critical shear strain rates of particles are estimated in Fig. 8(a). Then, the correlation between the particle Reynolds number and the critical Shields number with $Re_p \in [0.093, 10.7]$ in log–log coordinates (base 10) is shown in Fig. 8(b). For stainless-steel particles, there is a decrease in the critical Shields number as the particle Reynolds number increases, and the correlation can be described as follows, with R^2 = 0.98.

$$\theta_c = 0.242\ Re_p^{-0.728} \tag{8}$$

The slope of −0.728 we obtained is different from the slope of −0.2306 reported by Yalin *et al.* [22] in log–log coordinates. Given that Yalin *et al.* [22] has focused on sand (s = 1.65), this deviation may be due to the high densities of stainless-steel particles. Furthermore, we observe that the critical Shields numbers of low-density particles (s = 2.7) are close to the Shields curve for sand reported by Yalin *et al.* [22]. Besides, with the increase of Re_p, the critical Shields numbers of particles are gradually approaching 0.05, in agreement with the findings of research [20–22].

4.4. Effect of bed thickness

The temporal evolutions of bed removal radii at different bed thicknesses in our experiments are given in Fig. 9(a). It is obvious that the critical removal radius of bed is negatively correlated with the bed thickness, and it takes less time to reach a stable state for a thicker bed.

The critical Shields numbers are collected at different bed thicknesses, see Fig. 9(b). The critical Shields number for the "near zero thickness" case is about 0.05, which is in good agreement with data from published studies [20–22]. A linear correlation between the critical Shields number and the bed thickness can be described as follows, with R^2 = 0.981 and δ in meter.

$$\theta_c = 10.5\ \delta + 0.05 \tag{9}$$

In Fig. 9(b), a slight deviation from the fitted line can be seen around δ = 0.004 m. To figure out the reason for this deviation, we display stable bed patterns for different bed thicknesses in Fig. 10.

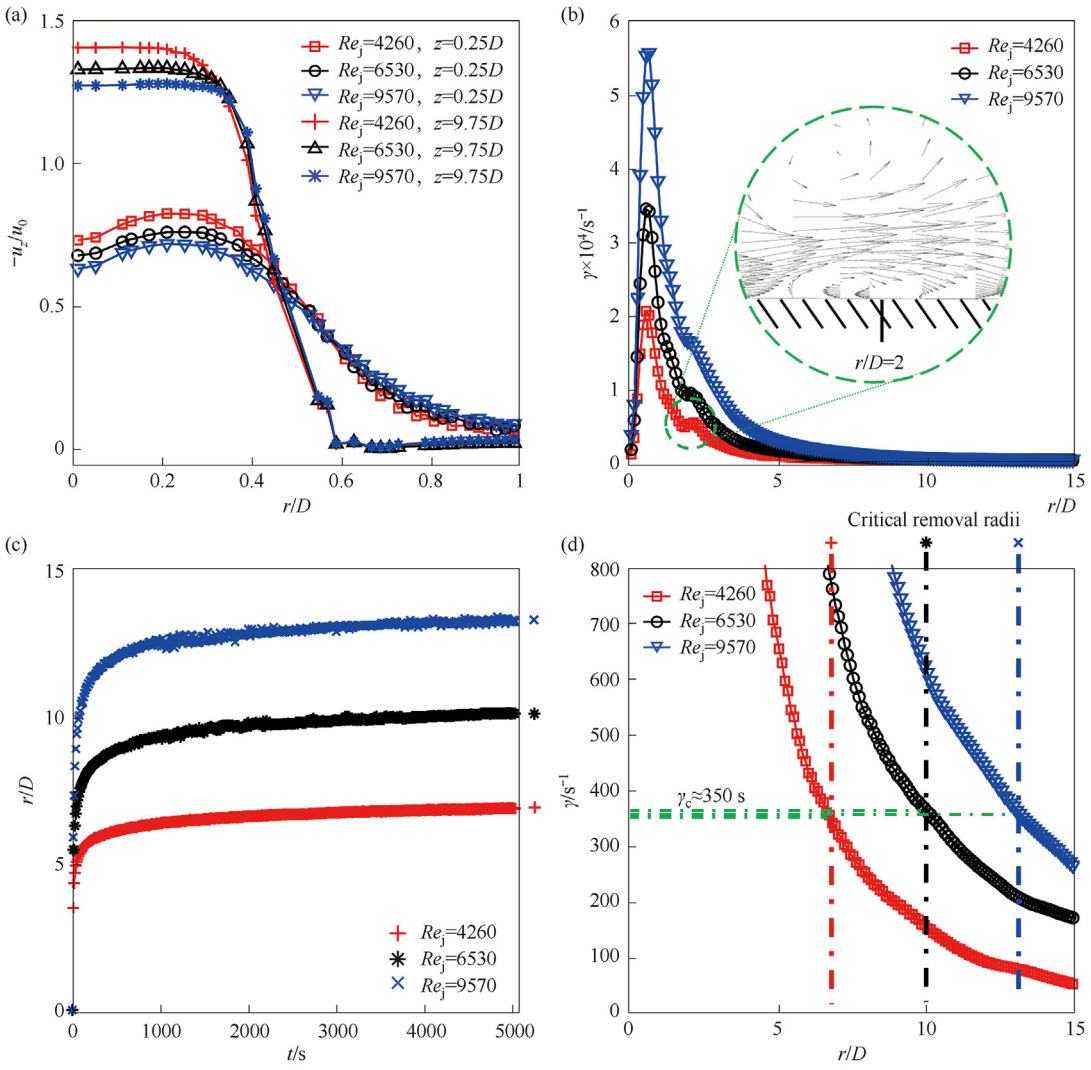

Fig. 6. (a) Simulated velocity profiles at $z/D = 0.25$ and $z/D = 9.75$; (b) simulated wall shear strain rate profiles; (c) experimental bed removal radii as a function of time for different Re_j; (d) estimation method of critical shear strain rates. $s = 7.04$, $d = 100$ μm, $\delta = 0.0003$ m.

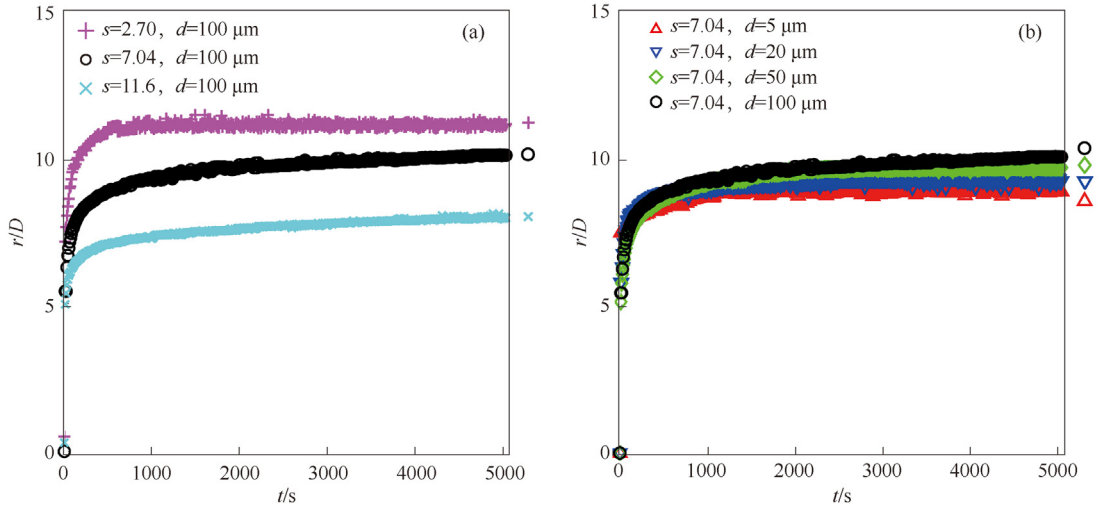

Fig. 7. Bed removal radii as a function of time for different (a) particle density, and (b) particle diameter. $Re_j = 6530$, $\delta = 0.0003$ m.

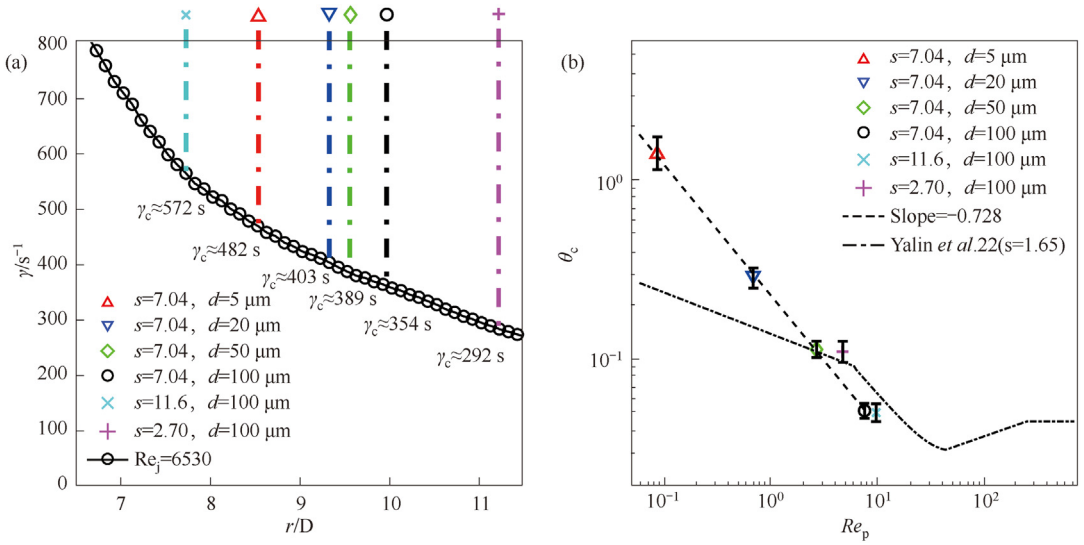

Fig. 8. (a) Estimated values of critical shear strain rates for different particles. (b) Correlation between particle Reynolds numbers and critical Shields numbers. Re_j = 6530, δ = 0.0003 m.

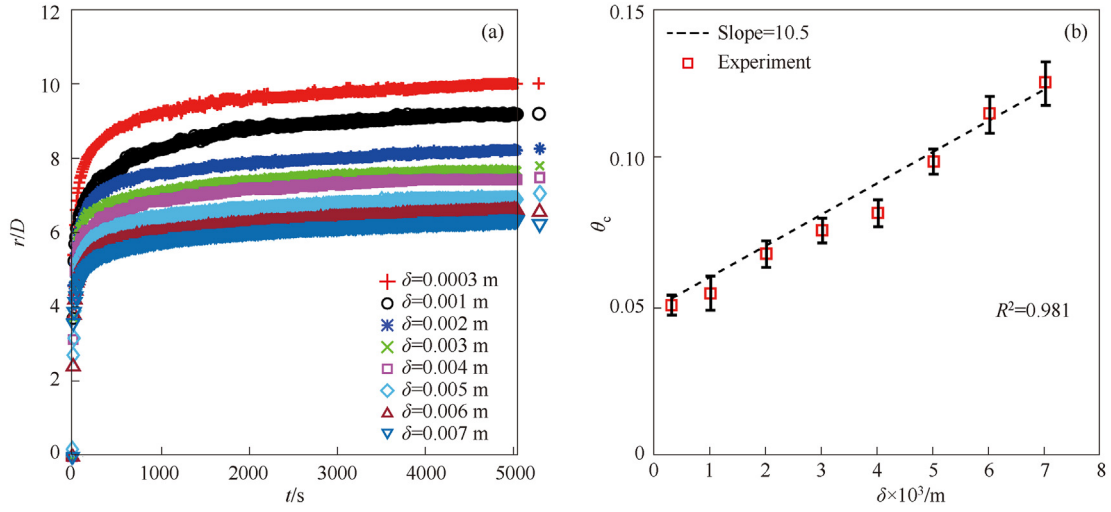

Fig. 9. (a) Bed removal radii as a function of time at different bed thicknesses. (b) Correlation between critical Shields numbers and bed thicknesses. Re_j = 6530, s = 7.04, d = 100 μm.

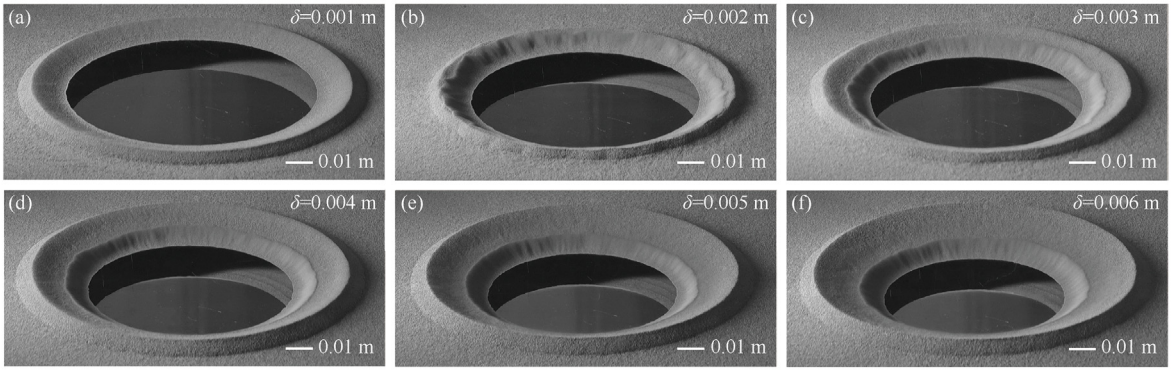

Fig. 10. Stable bed patterns at bed thickness of (a) 0.001 m; (b) 0.002 m; (c) 0.003 m; (d) 0.004 m; (e) 0.005 m; (f) 0.006 m. Re_j = 6530, s = 7.04, d = 100 μm.

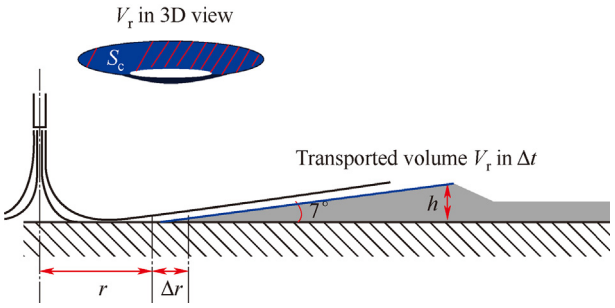

Fig. 11. Schematic diagram of bed load transport in an impinging jet on a horizontal surface. The bed and jet are scaled non-proportionally.

The circular bed formed by the jet, called as "dune", is very smooth when $\delta = 0.001$ m. The peak boundary of the dune become fuzzy at $\delta = 0.002$ m, accompanied by a reduction in its diameter, because a second dune is forming. A pair of dunes can be clearly seen for the case of $\delta = 0.003$ m. After δ reaches 0.004 m, the two peak boundaries of the two dunes become quite clear. With increasing δ from 0.004 to 0.006 m, the diameter of the peak boundary of the outer dune is almost constant, but the diameter of the base boundary of the inner dune quickly decreases from 15D to 13D. Therefore, we consider the deviation in Fig. 9(b) is due to the dynamic generation process of the inner dune.

4.5. Bed load transport rate

In shear flows, the transported bed on a horizontal surface consists of two main parts: the bed load (particles moving by rolling, sliding, or in short jumps) and the suspended load (particles entrained in the flow closely above the bed) [23]. According to the review of Nielsen [24], even under high shear conditions ($\theta \approx 1$), the proportion of suspended load transport in the total sediment transport is not more than 20%. Based on our visual observations, almost all particles in this study moved as bed load when $\delta = 0.0003$ m, and only cases with initial bed thicknesses of 0.0003 m are included in this section.

Fig. 11 shows a schematic diagram of the bed load transport, and the transported bed during unit time Δt is marked in blue. When r/D is in the range of 3 to 8 and initial bed thickness δ is 0.0003 m, our experimental results show that the inner stacking angle of the dune in jet flows is about 7°, and the bed stacking height h is approximately equal to 0.001 m. Then the transported volume V_r can be estimated based on the change of removal radius Δr per unit time Δt and the lateral surface area S_c of the frustum of cone. And the mass transport rate q_m of bed load per unit width at characteristic radius $r + \Delta r/2$ is calculated by dividing the transported mass by the characteristic perimeter. The calculation equation is as follows:

$$q_m = \rho_b \frac{V_r}{\Delta t \times 2\pi(r+\Delta r/2)} \approx \rho_b \frac{\Delta r \times \sin(7°) \times S_c}{\Delta t \times 2\pi(r+\Delta r/2)} = \rho_b \frac{\Delta r \times \sin(7°) \times \pi \frac{h}{\sin(7°)} \left[r + \left(r + \frac{h}{\tan(7°)} \right) \right]}{\Delta t \times 2\pi(r+\Delta r/2)} \quad (11)$$

where ρ_b is the packing density of bed and be known as $0.63\rho_s$ according to the random close packing [25], and $\Delta t = 1$ s is the sampling interval of the camera in this section.

The measured bed load transport rates q_m are shown in Fig. 12. Each set of data contains the results of three repeated experiments, and they are presented with the same mark. Because the bed removal process was random and rapid (took only 1 to 2 s) during the interval when r/D increased from 0 to 3, we collected data starting from the location $r/D = 3$.

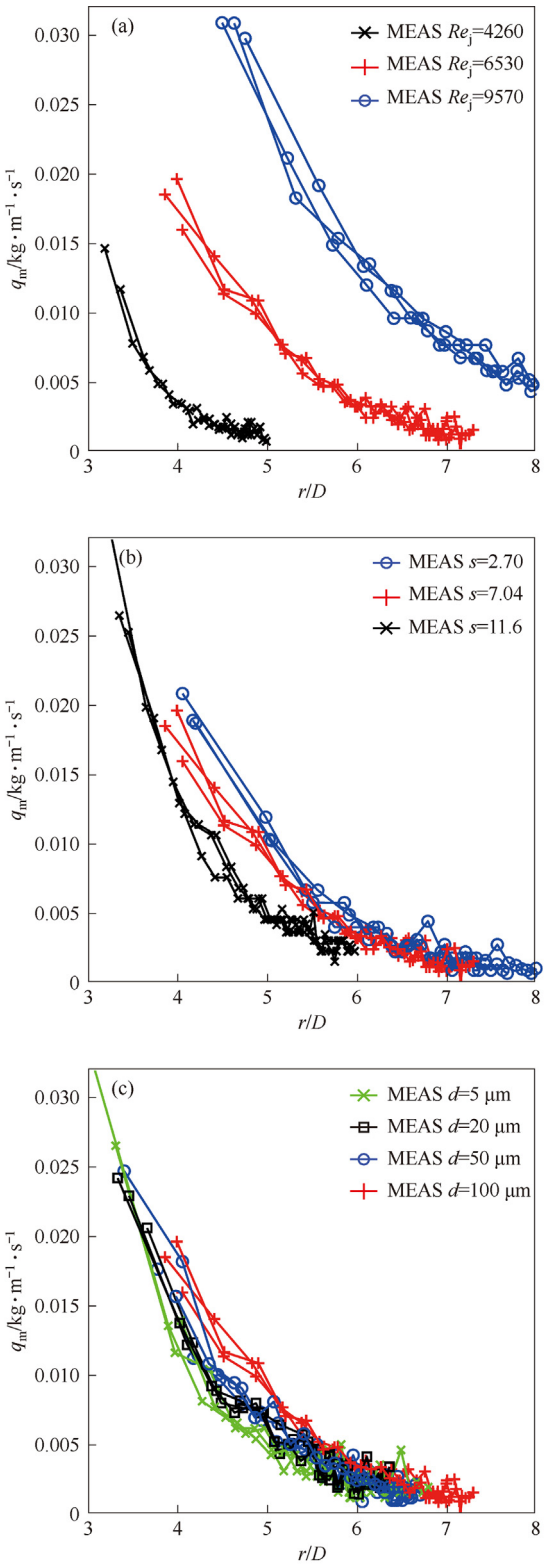

Fig. 12. Measured bed load transport rates for different (a) jet intensity; (b) particle density; (c) particle diameter. Default values without mention: $Re_j = 6530$, $s = 7.04$, $d = 100$ μm, $\delta = 0.0003$ m.

For all the cases in Fig. 12, the transport rates decline with the increase of r/D ranging from 3 to 8. Fig. 12(a) shows that the jet Reynolds number has significant effect on the transport rate. For example, q_m with Reynolds number of 4260 and 9570 at $r/D = 5$ is 0.001 and 0.024 $kg \cdot m^{-1} \cdot s^{-1}$, respectively. This indicates that the particle motion exhibits a sensitive response to the increase in agitating power resulting from enhanced jet intensity. The curves resembling Fig. 6(d) suggest a correlation between transport rate and shear stress. The effect of particle density is shown in Fig. 12(b), and particles with lower density are transported at a higher rate at the same location. Compared with the first two factors, the particle diameter has a limited effect on the mass transport rate.

To our knowledge, no model for particle transport rates in vertical wall jets has been reported in the literature. We have therefore drawn inspiration from models for particle transport in river channels [26–28], specifically the one reported by Kleinhans *et al.* [29] for initial transport along coastlines. Our experimental data guided the necessary adaptations to this model.

For the prediction of bed load transport on a horizontal surface, many empirical models [26–29] were developed, and the general equation of the mass transport rate per unit of width can be written as follows:

$$q_m = \begin{cases} \alpha(\theta - \theta_c)^{\beta} \times \rho_s d \sqrt{\dfrac{\rho_s - \rho}{\rho} g d}, & \theta \geq \theta_c \\ 0, & \theta < \theta_c \end{cases} \tag{12}$$

where α and β are empirical dimensionless constants. For similar particle motion starting from rest in this study, Kleinhans *et al.* [29] have reported one correlation for the incipient motion of particles on the coastline, with $\alpha = 1$ and $\beta = 1.5$.

The measured dimensionless transport rates $q_m \Big/ \rho_s d \sqrt{(\rho_s - \rho) g d / \rho}$ (denoted as MEAS $\alpha(\theta - \theta_c)^{\beta}$) in our experiments as a function of $(\theta - \theta_c)$ are shown in Fig. 13. We consider the coefficient β as 1.5, following most existing models [26–29], and then a fitted value of 1.5 is obtained for α, with $R^2 = 0.96$. A revised model is proposed as follows:

$$q_m = \begin{cases} 1.5(\theta - \theta_c)^{1.5} \times \rho_s d \sqrt{\dfrac{\rho_s - \rho}{\rho} g d}, & \theta \geq \theta_c \\ 0, & \theta < \theta_c \end{cases} \tag{13}$$

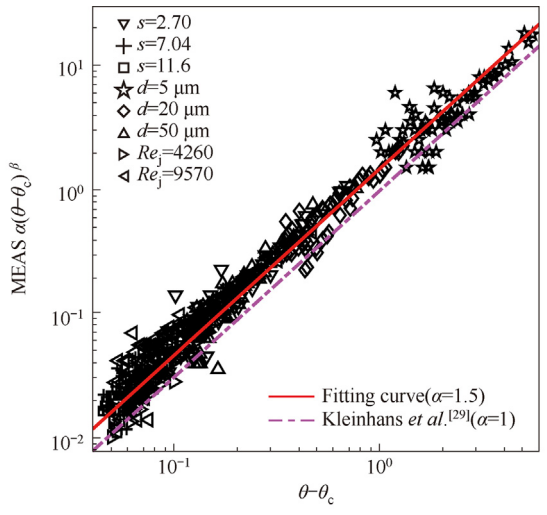

Fig. 13. Correlation between measured dimensionless transport rates $\alpha(\theta - \theta_c)^{\beta}$ and $\theta - \theta_c$. Default values without mention: $Re_j = 6530$, $s = 7.04$, $d = 100$ μm, $\delta = 0.0003$ m.

5. Conclusions

We studied the removal processes of horizontal beds, consisting of micron-sized spherical metal particles, driven by vertical submerged water jets. Various factors such as jet intensity, particle density, particle diameter, and bed thickness were considered, and single-phase large eddy simulations were used to predict the shear stress acting on particles. The main conclusions are summarized as follows:

(1) The critical Shields number was found to be intricately related to properties of particles, and independent of jet intensity. As particle Reynolds number increased, we observed that the critical Shields numbers of particles gradually approached 0.05, which was consistent with the published results on sediment transport. A new Shields number curve for stainless-steel particles with diameter $d \leq 100\,\mu$m is proposed.
(2) To verify the simulations, the velocity profiles measured using the PIV technique and the wall shear stain rate profiles measured using the electrochemical diffusion technique were cited. The simulated results matched well with the experimental data reported in the literature.
(3) Based on the bed load transport models and our experiment results, we proposed a revised transport rate model. With the simulated wall shear stress profiles, the revised model could accurately predict the bed load transport rates of the thin beds under the impinging jet.

This research could be extended in at least two ways: studying the bed motion under the jet with incident angles, and carrying out larger scale experiments. They aim at the prediction of transport in side-entry jets and larger containers. The numerical simulations of solid-liquid two-phase flow, as well as hybrid LES and RANS approach, will be our future research directions. The experimental results in this study can also provide reference for numerical model validation.

CRediT Authorship Contribution Statement

Han Peng: Writing – original draft. Xinliang Jia: Software. Xiaofang Guo: Methodology. Yubo Jiang: Resources. Zhipeng Li: Writing – review & editing. Zhengming Gao: Supervision. J.J. Derksen: Writing – review & editing.

Declaration of Competing Interest

The authors declare that they have no known competing financial interests or personal relationships that could have appeared to influence the work reported in this paper.

Acknowledgements

This research did not receive any specific grant from funding agencies in the public, commercial, or not-for-profit sectors.

Nomenclature

C_w	a coefficient in the simulation
D, D_o	inner and outer diameter of nozzle outlet, m
d	average particle diameter, μm
g	gravitational acceleration, $m \cdot s^{-2}$
H	liquid height in the square glass tank, m
h	stacking height of bed, m
L	side length of the square glass tank, m

p	the pressure in the simulation, $N \cdot m^{-2}$
q_m	mass transport rate of bed load per unit width, $kg \cdot m^{-1} \cdot s^{-1}$
Re_j	jet Reynolds number
Re_p	particle Reynolds number
r	radius of the lower edge of the impact pit, m
S_c	lateral surface area of the frustum of cone, m^2
S_{ij}	deformation tensor of the resolved field in the simulation, s^{-1}
S_{ij}^d	traceless symmetric part of the square of the velocity gradient tensor, s^{-2}
s	submerged specific weight of sediment, $s = \rho_s/\rho - 1$
t	duration of jet, s
U_f, U_r	frictional velocity and flow velocity around particles, $m \cdot s^{-1}$
u_0	mean flow velocity within the tube, $m \cdot s^{-1}$
u_i, u_j	the velocity component in different coordinate directions in the simulation, $m \cdot s^{-1}$
u_r, u_x	transverse velocity, $m \cdot s^{-1}$
u_z	streamwise velocity, $m \cdot s^{-1}$
V	volume of a computational cell, m^3
V_r	transported volume in unit time, m^3
y	distance to the closest wall, m
y^+	dimensionless distance to the closest wall, $y^+ = \rho y U_f/\mu$
α, β	empirical constant for the bed load transport model
γ, γ_c	shear strain rate and critical shear strain rate, s^{-1}
Δ	filter width in the simulation, m
Δr	change of the removal radii, m
Δt	time step or interval, s
Δx_{max}	maximum grid spacing in the simulation, m
δ	initial bed thickness, m
θ, θ_c	Shields number and critical Shields number, $\theta = \tau/[g(\rho_s - \rho)d]$
κ	von Karman constant
μ	dynamic viscosity of water, $N \cdot s \cdot m^{-2}$
ν, ν_t	kinematic viscosity of the liquid and the eddy viscosity, $m^2 \cdot s^{-1}$
ρ, ρ_b, ρ_s	density of liquid, packing density of particles, and density of particles, $kg \cdot m^{-3}$
σ	the sub-grid scale stress tensor in the simulation, $N \cdot m^{-2}$
τ, τ_c	shear stress and critical shear stress, $N \cdot m^{-2}$

Abbreviations

j	jet
MEAS	measured values by experiments
PIV	measured values by using particle image velocimetry
p	particle
SIM	simulated values
s	sediment

Supplementary Material

Supplementary data to this article can be found online at https://doi.org/10.1016/j.cjche.2025.02.017.

References

[1] P.C. Upson, Highly active liquid waste management at Sellafield, *Prog. Nucl. Energy* 13 (1) (1984) 31–47.
[2] R. Natarajan, Reprocessing of spent nuclear fuel in India: present challenges and future programme, *Prog. Nucl. Energy* 101 (2017) 118–132.
[3] P.K. Wattal, Back end of Indian nuclear fuel cycle-a road to sustainability, *Prog. Nucl. Energy* 101 (2017) 133–145.
[4] A. Shields, Anwendung der Aehnlichkeitsmechanik und der Turbulenzforschung auf die Geschiebebewegung, PhD Thesis. Technical University, Berlin, 1936..
[5] P.A. Mantz, Incipient transport of fine grains and flakes by fluids: Extended shields diagram, *J. Hydraul. Div.* 103 (6) (1977) 601–615.
[6] R.M. Young, M.J. Hargather, G.S. Settles, Shear stress and particle removal measurements of a round turbulent air jet impinging normally upon a planar wall, *J. Aerosol Sci.* 62 (2013) 15–25.
[7] D.I. Wilson, P. Atkinson, H. Köhler, M. Mauermann, H. Stoye, K. Suddaby, T. Wang, J.F. Davidson, J.P. Majschak, Cleaning of soft-solid soil layers on vertical and horizontal surfaces by stationary coherent impinging liquid jets, *Chem. Eng. Sci.* 109 (2014) 183–196.
[8] H.P. Wang, Z.X. Yang, B.L. Li, S.Z. Wang, Predicting the near-wall velocity of wall turbulence using a neural network for particle image velocimetry, Phys. Fluids 32 (11) (2020) 115105.
[9] D.J. Phares, G.T. Smedley, R.C. Flagan, The wall shear stress produced by the normal impingement of a jet on a flat surface, *J. Fluid Mech.* 418 (2000) 351–375.
[10] M. Kristiawan, K. Sodjavi, B. Montagné, A. Meslem, V. Sobolik, Mass transfer and shear rate on a wall normal to an impinging circular jet, *Chem. Eng. Sci.* 132 (2015) 32–45.
[11] M. El Hassan, H.H. Assoum, R. Martinuzzi, V. Sobolik, K. Abed-Meraim, A. Sakout, Experimental investigation of the wall shear stress in a circular impinging jet, Phys. Fluids 25 (7) (2013) 077101.
[12] K. Sodjavi, B. Montagné, P. Bragança, A. Meslem, P. Byrne, C. Degouet, V. Sobolik, PIV and electrodiffusion diagnostics of flow field, wall shear stress and mass transfer beneath three round submerged impinging jets, *Exp. Therm. Fluid Sci.* 70 (2016) 417–436.
[13] A.D. Eisner, The impact of the surface macro-roughness on the surface shear stress and rate under the oblique linear cylindrical nozzle jet as pertinent to particles detachment, *J. Aerosol Sci.* 102 (2016) 16–28.
[14] F. Nicoud, F. Ducros, Subgrid-scale stress modelling based on the square of the velocity gradient tensor, *Flow Turbul. Combust.* 62 (3) (1999) 183–200.
[15] A. Fluent, Ansys Fluent Theory Guide, ANSYS Inc., Pittsburgh, 2021, pp. 116–129.
[16] T.J. Atherton, D.J. Kerbyson, Size invariant circle detection, *Image Vis Comput.* 17 (11) (1999) 795–803.
[17] J.J. Derksen, Simulations of granular bed erosion due to a mildly turbulent shear flow, *J. Hydraul. Res.* 53 (5) (2015) 622–632.
[18] A. Meslem, V. Sobolik, F. Bode, K. Sodjavi, Y. Zaouali, I. Nastase, C. Croitoru, Flow dynamics and mass transfer in impinging circular jet at low Reynolds number. Comparison of convergent and orifice nozzles, *Int. J. Heat Mass Tran.* 67 (2013) 25–45.
[19] M.J. Tummers, J. Jacobse, S.G.J. Voorbrood, Turbulent flow in the near field of a round impinging jet, *Int. J. Heat Mass Tran.* 54 (23–24) (2011) 4939–4948.
[20] J. Fredsøe, R. Deigaard, Mechanics of Coastal Sediment transport, World Scientific, Singapore, 1992, pp. 201–205.
[21] Z.X. Cao, G. Pender, J. Meng, Explicit formulation of the shields diagram for incipient motion of sediment, *J. Hydraul. Eng.* 132 (10) (2006) 1097–1099.
[22] M.S. Yalin, A.F. Da Silva, Fluvial processes, IAHR, Delf, 2001.
[23] F. Engelund, J. Fredsøe, A sediment transport model for straight alluvial channels, *Hydrol. Res.* 7 (5) (1976) 293–306.
[24] P. Nielsen, Coastal Bottom Boundary Layers and Sediment Transport, World Scientific, Singapore, 1992, pp. 109–115.
[25] R.A. Bagnold, The flow of cohesionless grains in fluids, *Philos. Trans. R. Soc. A.* 249 (964) (1956) 235–297.
[26] E. Meyer-Peter, R. Mueller, Formulas for bed-load transport, *Proc. 2nd Int. Ass. Hydraul. Struct. Res.* 6 (7–9) (1948) 39–64.
[27] R. Fernandez Luque, R. Van Beek, Erosion and transport of bed-load sediment, *J. Hydraul. Res.* 14 (2) (1976) 127–144.
[28] P.L. Wiberg, J. Dungan Smith, Model for calculating bed load transport of sediment, *J. Hydraul. Eng.* 115 (1) (1989) 101–123.
[29] M.G. Kleinhans, B.T. Grasmeijer, Bed load transport on the shoreface by currents and waves, *Coast. Eng.* 53 (12) (2006) 983–996.